

The resolved size and structure of hot dust in the immediate vicinity of AGN

GRAVITY Collaboration: J. Dexter^{1,23}, J. Shangguan¹, S. Hönig⁵, M. Kishimoto⁶, D. Lutz¹, H. Netzer⁸, R. Davies¹, E. Sturm¹, O. Pfuhl^{1,15}, A. Amorim^{18,20}, M. Bauböck¹, W. Brandner²¹, Y. Clénet², P. T. de Zeeuw^{1,16}, A. Eckart^{3,17}, F. Eisenhauer¹, N.M. Förster Schreiber¹, F. Gao¹, P. J. V. Garcia^{14,19,20}, R. Genzel^{1,4}, S. Gillessen¹, D. Gratadour², A. Jiménez-Rosales¹, S. Lacour^{2,1,15}, F. Millour⁷, T. Ott¹, T. Paumard², K. Perraut¹², G. Perrin², B. M. Peterson^{9,10,11}, P. O. Petrucci¹², M. A. Prieto²², D. Rouan², M. Schartmann¹, T. Shimizu¹, A. Sternberg^{8,13}, O. Straub¹, C. Straubmeier³, L. J. Tacconi¹, K. Tristram¹⁴, P. Vermot², I. Waisberg^{1,24}, F. Widmann¹, and J. Woillez¹⁵

¹ Max Planck Institute for Extraterrestrial Physics (MPE), Giessenbachstr.1, 85748 Garching, Germany

² LESIA, Observatoire de Paris, Université PSL, CNRS, Sorbonne Université, Université de Paris, 5 place Jules Janssen, 92195 Meudon, France

³ I. Institute of Physics, University of Cologne, Zùlpicher Straße 77,50937 Cologne, Germany

⁴ Departments of Physics and Astronomy, Le Conte Hall, University of California, Berkeley, CA 94720, USA

⁵ Department of Physics and Astronomy, University of Southampton, Southampton, UK

⁶ Department of Astrophysics and Atmospheric Sciences, Kyoto Sangyo University, Japan

⁷ Université Côte d'Azur, Observatoire de la Côte d'Azur, CNRS, Laboratoire Lagrange, Nice, France

⁸ School of Physics and Astronomy, Tel Aviv University, Tel Aviv 69978, Israel

⁹ Department of Astronomy, The Ohio State University, Columbus, OH, USA

¹⁰ Center for Cosmology and AstroParticle Physics, The Ohio State University, Columbus, OH, USA

¹¹ Space Telescope Science Institute, Baltimore, MD, USA

¹² Univ. Grenoble Alpes, CNRS, IPAG, 38000 Grenoble, France

¹³ Center for Computational Astrophysics, Flatiron Institute, 162 5th Ave., New York, NY 10010, USA

¹⁴ European Southern Observatory, Casilla 19001, Santiago 19, Chile

¹⁵ European Southern Observatory, Karl-Schwarzschild-Str. 2, 85748 Garching, Germany

¹⁶ Sterrewacht Leiden, Leiden University, Postbus 9513, 2300 RA Leiden, The Netherlands

¹⁷ Max Planck Institute for Radio Astronomy, Bonn, Germany

¹⁸ Universidade de Lisboa - Faculdade de Ciências, Campo Grande, 1749-016 Lisboa, Portugal

¹⁹ Faculdade de Engenharia, Universidade do Porto, rua Dr. Roberto Frias, 4200-465 Porto, Portugal

²⁰ CENTRA - Centro de Astrofísica e Gravitação, IST, Universidade de Lisboa, 1049-001 Lisboa, Portugal

²¹ Max Planck Institute for Astronomy, Königstuhl 17, 69117, Heidelberg, Germany

²² Instituto de Astrofísica de Canarias (IAC), E-38200 La Laguna, Tenerife, Spain

²³ JILA and Department of Astrophysical and Planetary Sciences, University of Colorado, Boulder, CO 80309, USA

²⁴ Department of Particle Physics & Astrophysics, Weizmann Institute of Science, Rehovot 76100, Israel

February 21, 2022

ABSTRACT

We use VLTI/GRAVITY near-infrared interferometry measurements of 8 bright, Type 1 AGN to study the size and structure of hot dust heated by the central engine. We partially resolve each source, and report Gaussian FWHM sizes in the range 0.3–0.8 milliarcseconds. In all but one object, we find no evidence for significant elongation or asymmetry (closure phases $\lesssim 1^\circ$). The effective physical radius increases with bolometric luminosity as found from past reverberation and interferometry measurements. The measured sizes for Seyfert galaxies are systematically larger than for the two quasars in our sample when measured relative to the previously reported $R \sim L^{1/2}$ relationship explained by emission at the sublimation radius. This could be evidence of evolving near-infrared emission region structure as a function of central luminosity.

Key words. galaxies: active, galaxies: nuclei, galaxies: Seyfert, quasars, techniques: interferometric

1. Introduction

The spectral energy distributions (SEDs) of AGN show an excess in the near-infrared (NIR) due to thermal emission from hot dust grains with a color temperature $T_{\text{color}} \simeq 1000 - 1500\text{K}$. The dust luminosity and temperature is explained as reprocessing of emission from the central accretion disk (e.g., Rieke 1978). In the standard unification paradigm of AGN, dust distributed in a flattened, large covering factor, parsec-scale “torus” obscures the

view of the broad emission lines and central accretion disk for large viewing angles (Antonucci 1993; Urry & Padovani 1995). The NIR radiation might then arise at the inner edge near the sublimation radius, where irradiation from the center is strongest and dust temperature the highest. The physical origin of such a structure remains unclear. Support by gas pressure would require a sound speed far in excess of the Keplerian speed at that dis-

tance from the central black hole. Alternatives include radiation or magnetic pressure support, usually in the form of an outflow.

Mid-infrared interferometry presents a challenge to the torus paradigm. Many objects show an unresolved core, consistent with an origin in the inner part of the torus. At the same time, a significant fraction of the total flux may originate in the polar region on pc and larger scales, attributed to dusty outflows from the center (e.g., López-Gonzaga et al. 2016; Hönig & Kishimoto 2017). It remains unclear whether this material is producing significant obscuration of the central source. The first resolved image of hot dust found from GRAVITY observations of NGC 1068 shows a size consistent with that expected for the sublimation radius, but in a geometrically thin ring geometry (GRAVITY Collaboration: Pfuhl et al., submitted). An additional obscuring structure is required to explain the absence of broad emission lines.

Continuum reverberation experiments find correlated variability between the optical and NIR emission with a lag consistent with reprocessing. The inferred emission radius scales with luminosity as $R \sim L^{1/2}$ (Suganuma et al. 2006; Koshida et al. 2014), as expected if hot dust radiation peaks near the sublimation radius where the central engine radiation is weak enough for dust to survive (e.g., Barvainis 1987). The normalization of the relation is smaller than predicted, which may be due to the presence of large, graphite dust grains (Kishimoto et al. 2007).

The inferred sub-pc (\lesssim milliarcsecond, mas) scales are too compact to be spatially resolved with single telescopes. NIR interferometry, mostly with the Keck Interferometer (Swain et al. 2003; Kishimoto et al. 2009, 2011a) as well as the VLT Interferometer instrument AMBER (Weigelt et al. 2012) have measured compact sizes associated with partially resolved sources. The size measurements are consistent with an origin at the sublimation radius as found from reverberation.

The second generation VLTI instrument GRAVITY has vastly improved sensitivity and coverage as a result of combining light from all 4 UT telescopes, resulting in a 6 baseline array (Gravity Collaboration et al. 2017). We use data from our ongoing AGN observing program to measure sizes for a sample of 8 of the brightest type 1 AGN, nearly doubling the sample for which NIR interferometry is available. We describe the data acquisition and selection procedure (section 2) and fitting methods used to measure sizes from both continuum and differential visibilities (section 3). All AGN are partially resolved, with consistent results from both methods (section 4). We find similar angular sizes for objects of similar flux but spanning four orders of magnitude in luminosity, meaning that the physical size of the hot dust emission increases with luminosity. The two luminous quasars in our sample are more compact than the Seyfert 1s observed. All measured sizes are broadly consistent with the radius-luminosity relation determined using previous NIR interferometry measurements. We discuss the implications of our results in terms of dust emissivity, composition, and the relation of the hot dust emission to that of the broad emission line region (section 5).

2. Observations, Data Reduction, and Data Selection

2.1. Observations

The main science goal of our GRAVITY AGN observing program is to spatially resolve the broad emission line region, which has recently been achieved with observations of the quasar 3C 273 (Gravity Collaboration et al. 2018). Targets are selected as

the brightest Type 1 AGN on the sky visible from the VLTI. For BLR science we require deep integrations and repeated observations over many nights, with less emphasis on observing calibrators.

In the past 2 years we have successfully observed 8 Type 1 AGN over 26 nights¹. Details of the targets and observations are given in Table 1. For each observation, we first close the loop of the MACAO visible AO systems on the visible AGN source with each of the 4 UT telescopes. The AGN is then acquired on the GRAVITY acquisition camera and we place both the GRAVITY fringe tracking (FT) and science channel (SC) fibers on the AGN (observing on-axis), and split the light between the two detectors. Once fringes are acquired, we collect exposures with coherent integrations of 3.3ms on the FT and 30s on the medium spectral resolution SC detector ($R \sim 500$). We record a sequence of exposures of 10 SC DITs each, interrupted by occasional sky exposures or calibrator observations. Even the brightest AGN are relatively faint in V, resulting in a poor AO correction even in exceptional conditions. Fringe tracking signal-to-noise is generally low ($\lesssim 3$) at 300 Hz but remains stable due to the excellent performance of the GRAVITY fringe tracker (Lacour et al. 2019).

2.2. Data Reduction

The data are reduced with the standard GRAVITY pipeline (Lapeyrere et al. 2014; Gravity Collaboration et al. 2017) in two separate modes. For the continuum FT visibility data we use the default pipeline settings. The low signal-to-noise and reduced SC visibility amplitude (loss of coherence) often result in the pipeline flagging SC DITs or entire exposures. In analyzing those data, we have found a substantial improvement in performance by retaining all data independent of fringe tracker signal-to-noise or V-factor and then averaging all DITs by the inverse variance of their differential phases (Gravity Collaboration et al. 2018). The differential phase is constructed by removing a mean and slope across the spectrum. We use a method where the mean and slope are computed separately for each spectral channel, excluding that channel itself from the measurement (Millour et al. 2008), as implemented in the GRAVITY pipeline. This method improves our differential phase precision by $\approx 10 - 20\%$.

2.3. Acquisition Camera Images and Photometry

We estimate the AGN H band magnitude using the GRAVITY acquisition camera. We fit a 2D Gaussian model to the image from each telescope in each exposure, and estimate the source flux as that integrated over the Gaussian model. We then flux calibrate using the same acquisition camera measurements of calibrator stars of known magnitude. The results are listed in Table 1. From looking at the same source on successive nights, or using different calibrators within the same night, we estimate the uncertainty in these measurements as 0.2 mag.

2.4. Data Selection

The fringe tracker (FT) keeps the record of fringe measurement in every DIT of 3.3 ms. The group delay and phase delay are calculated in real time to track the variation of the optical path differences of the baselines. The fringe tracker stabilizes the fringe to allow long integrations of the science channel. If the track-

¹ Observations were done using the ESO Telescopes at the La Silla Paranal Observatory programme IDs 099.B-0606, 0100.B-0582, 0101.B-0255, 0102.B-0667, 1103.B-0626.

Source	Obs. Date	Int. Time (min)	Seeing (")	Coherence time (ms)	Strehl	H	K	V
PDS 456	2018-08-26	65	0.51-0.85	4.8-8.3	0.03-0.14	11.3	10.2	14.5
	2018-08-27	40	0.40-0.50	4.0-6.2	0.18-0.23	11.7	10.7	
NGC 3783	2018-01-07	80	0.40-0.70	5.7-10.9	0.03-0.07	10.8	9.8	13.4
	2018-01-08	80	0.47-0.73	5.8-10.5	0.01-0.03	10.8	9.8	
	2018-05-31	105	0.38-0.61	2.5-4.8	0.10-0.27	10.6	9.8	
	2019-02-16	186	0.5-0.9	6.0-13.8	0.09-0.22	11.0	10.2	
	2019-03-31	120	0.4-0.6	3.2-7.0	0.03-0.20	...	10.2	
3C 273	2017-07-07	40	0.44-0.77	4.6-6.5	0.06-0.11	10.9	...	12.9
	2018-01-08	40	0.44-0.59	6.9-9.0	0.03-0.13	10.9	10.0	
	2018-05-30	90	0.48-0.68	2.9-4.1	0.05-0.15	11.0	10.1	
Mrk 509	2017-08-04	60	0.31-0.56	5.5-8.5	0.10-0.16	11.7	...	13.5
	2017-08-05	55	0.46-0.71	6.5-8.5	0.09-0.16	11.6	10.9	
	2017-08-08	30	0.29-0.48	9.0-10.8	0.23-0.28	11.6	10.7	
	2018-08-26	20	0.61-0.80	7.5-8.1	0.08-0.13	11.4	10.7	
NGC 1365	2018-01-07	15	0.54-0.65	6.6-10.9	0.02-0.03	10.9	10.0	
	2018-01-08	15	0.64-0.78	4.8-6.4	0.06-0.08	10.8	...	
3C 120	2018-11-20	20	0.35-0.56	4.1-5.7	0.05-0.13	11.4	11.6	15.1
IRAS 09149-6206	2018-11-20	65	0.64-1.03	3.7-4.0	0.07-0.13	10.9	9.8	12.3
	2019-02-16	96	0.5-1.2	5.7-9.2	0.04-0.14	10.5	9.7	
Mrk 335	2018-11-20	5	0.48	8.2	0.05	11.0	11.2	13.9
	2019-07-15	50	0.5-0.9	1.8-3.8	0.03-0.08	10.9	11.0	

Table 1. Observation epochs, total integration time on source, seeing and coherence time conditions reported by the DIMM, and Strehl ratios and H band aperture magnitudes obtained from the GRAVITY acquisition camera (50 mas FWHM aperture). The H and K band magnitudes were flux calibrated using Simbad H magnitudes of calibrator sources, and are only reported when a calibrator was observed. A typical uncertainty is 0.2 (H) and 0.3 (K) mag. The K magnitudes measured for 3C 120 and Mrk 335 are likely much more uncertain due to the very low Strehl ratios of those observations. The V magnitudes are taken from Simbad.

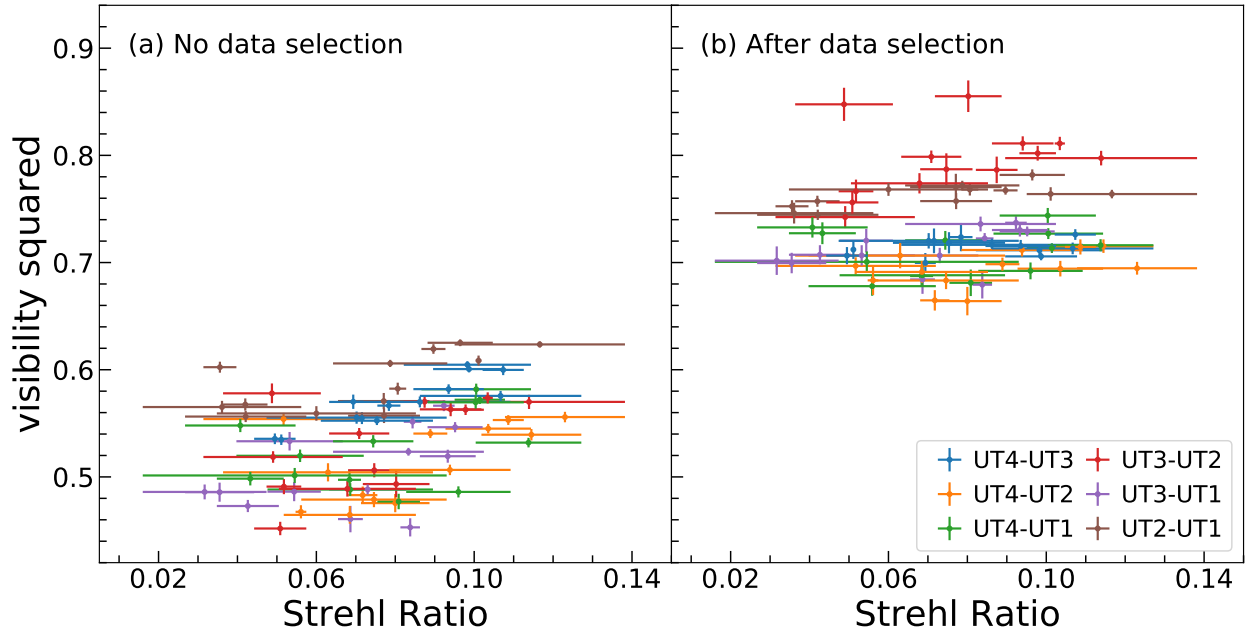


Fig. 1. Sample V^2 data of PDS 456 on 2018-08-27 before and after the data selection (group delay of $< 3\mu\text{m}$). Without the data selection (a), the averaged visibility squared data are ≤ 0.65 . There is a trend that visibility squared increases as the Strehl ratio increases for each baseline (e.g., UT4-UT3 and UT4-UT2). In contrast, the visibility squared reaches ≈ 0.8 after the data selection with no clear trend with Strehl ratio.

ing source is bright, most ($\geq 90\%$) of the FT group delays are $\leq 3\mu\text{m}$. However, the group delay of a considerable fraction (e.g., $\geq 50\%$) of the AGN fringe tracking data are usually much larger, resulting in considerable visibility loss. As an example in Figure 1, if we average all of the FT data, the visibility is much lower than unity. The correlation of the visibility squared with Strehl ratio implies that the visibility loss is likely affected by the atmosphere. When we only select the DITs with group de-

lay $< 3\mu\text{m}$ (rejecting 50 – 80% of DITs), the averaged visibility squared data are apparently improved. The correlation of visibility squared with Strehl ratio also vanishes. Although there are other effects possibly still keeping the visibility of the shortest baseline (UT3-UT2) below unity, the data selection based on the group delay apparently helps to improve the data.

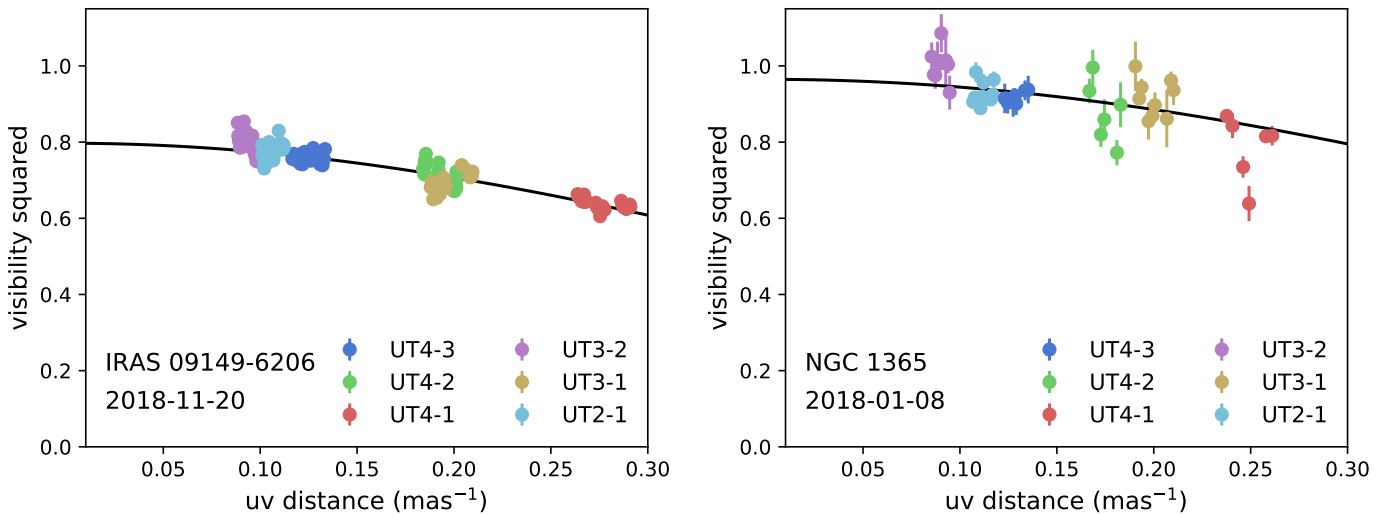


Fig. 2. Sample calibrated V^2 GRAVITY FT data as a function of baseline length for single epoch observations of two sources. The data pointed are color-coded by baseline. In both cases the sources are partially resolved, e.g. the visibilities fall with baseline length. For NGC 1365 on 2018-01-08, the V^2 approaches 1 at short baselines. For IRAS 09149-6206 on 2018-11-20, the short baselines remain significantly below $V^2 = 1$. The black lines are the best fitting 1D Gaussian models for each epoch.

3. Visibility model fitting

The typical size scales of hot dust in Type 1 AGN are $\lesssim 1$ mas while the maximum VLT/UT baseline resolution is ≈ 3 mas. As a result, all of our targets are only partially resolved. In that limit, all source models predict a similar trend of visibility amplitude (or V^2) with uv distance (spatial frequency). The observable property is then the characteristic size, related to the normalized second moment of the image (e.g., Lachaume 2003; Johnson et al. 2018). We adopt Gaussian source models throughout, and use both FT and SC data to measure the characteristic size (FWHM) of the hot dust emission region. We report angular measurements as Gaussian FWHM to avoid assumptions about the hot dust emission, e.g. that it comes from a thin ring near the sublimation radius as expected for an obscuring torus.

3.1. Continuum visibility fitting

Sample FT continuum V^2 data for two sources are shown in Figure 2, color-coded by baseline. In both cases the source is partially resolved, e.g. the visibilities fall with increasing baseline length. For NGC 1365, the visibility at zero baseline reaches unity, as it should for a model of a single compact source. In IRAS 09149-6206, it reaches only $V^2(0) \approx 0.8$. The zero baseline visibility varies between sources but also between exposures and nights for the same target. We attribute this to a likely coherence loss, although some fraction could also result from extended nuclear K band continuum emission. To deal with this effect, we fit for the zero baseline visibility along with the source size in each exposure for each object over all nights. The function fit is then,

$$V^2 = V_0^2 \exp(-2\pi^2 r_{uv}^2 \sigma^2), \quad (1)$$

for zero baseline visibility V_0 , size parameter σ in radians, and r_{uv} the baseline length in units of the observed wavelength λ . We report sizes after converting σ to FWHM measured in mas. Sample fits are shown as the solid lines in Figure 2, plotted against all data from one night for each source.

We determine average sizes and uncertainties from the median and rms scatter of all measured sizes over all exposures. To

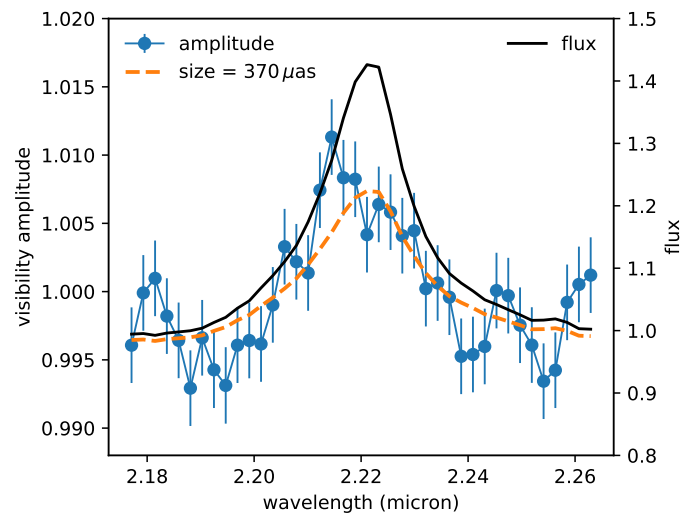


Fig. 3. Differential visibility amplitude vs. wavelength for PDS 456 from 2018-08-26 averaged over long baselines (blue circles and error bars) compared with the photometric flux. The orange curve shows a model of an unresolved BLR and a Gaussian continuum. The rise of the differential amplitude following the shape of the line is consistent with a partially resolved continuum, and its amplitude allows an independent measurement of its size.

account for correlated systematic errors in calibration, possibly related to AO performance and seeing conditions, we choose an uncertainty in the mean reduced by $\sqrt{N_{\text{epochs}}}$ (nights) rather than by the total number of exposures.

3.2. Differential visibility amplitude analysis

We also independently estimate hot dust continuum visibility amplitudes from the differential amplitude measured in the continuum and broad emission lines (Gravity Collaboration et al. 2018, low redshift Br γ in Seyfert galaxies or Pa α for quasars at $z > 0.1$). We normalize the visibility amplitude of each baseline and exposure to its median value, flatten slopes across the wave-

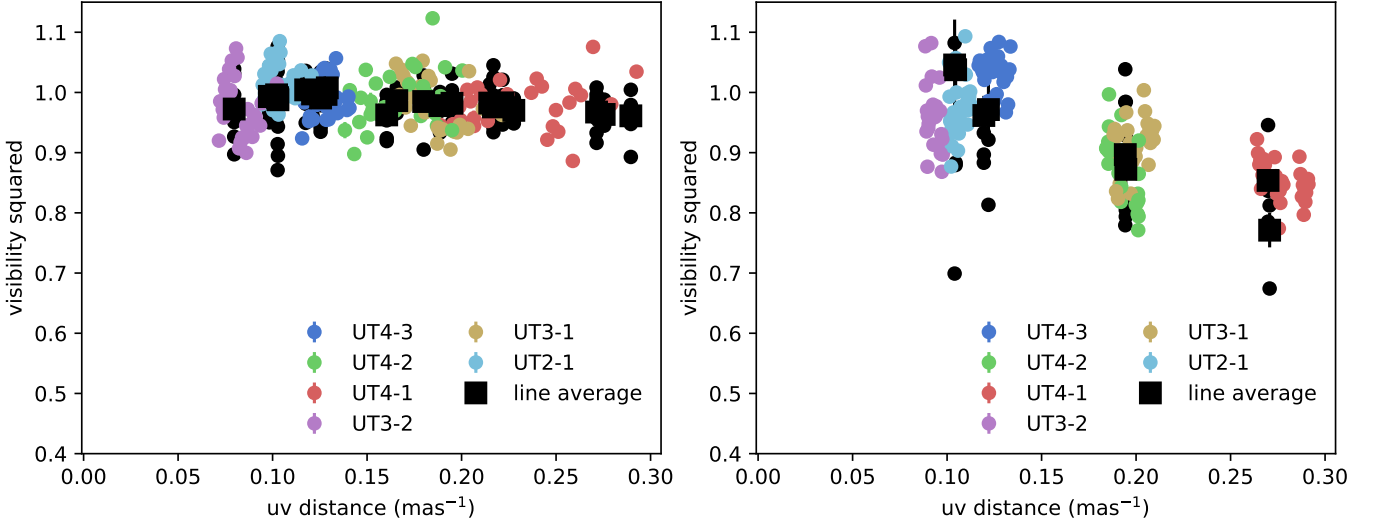


Fig. 4. Sample squared visibilities measured for FT (small circles colored by baseline) compared to those derived from SC differential amplitudes (black circles and averages as large squares) for 3C 273 (left) and IRAS 09149-6206 (right). The FT data have been divided by the best fitting zero baseline visibility, so that $V^2(0) = 1$. With that scaling, the two independent measurements are generally consistent.

length range by filtering out low frequency modes, and average over time with weights measured empirically in each exposure.

We construct the differential visibility by normalizing the visibility amplitude of each baseline. At a spectral channel with line flux f relative to a continuum level of 1, this is

$$v = \frac{1 + fV_l/V_c}{1 + f}, \quad (2)$$

where V_c and V_l are the continuum and line visibilities. The differential amplitude v at the line depends on the ratio V_l/V_c . In the partially resolved limit, that in turn measures the quadrature size difference between the line and continuum (Waisberg et al. 2017). For a larger (smaller) spectral line emission region, $|v|$ decreases (increases) at the line. We used these data previously to show conclusively that the hot dust emission size is larger than that of the Pa α BLR in 3C 273 (Gravity Collaboration et al. 2018). The continuum visibility is

$$\frac{V_c}{V_l} = \frac{f}{v(1 + f) - 1}. \quad (3)$$

We measure continuum visibilities V_c from the data (v, f) by assuming $V_l = 1$, e.g. that the broad emission lines are unresolved. The values f are taken from the photometric flux spectra, flattened to remove the instrument profile and averaged over the 4 UT telescopes and all exposures. They are then normalized to the continuum level. For 3C 273, we have found a BLR size from modeling differential phase data of $R_{\text{BLR}} = 46 \pm 10 \mu\text{as}$ (Gravity Collaboration et al. 2018). That size corresponds to a visibility $V_l \approx 0.996$ at a long VLTI baseline of 120m, justifying our approximation. We note that in general the BLR is found from reverberation to be a factor of $\approx 2 - 5$ smaller than the hot dust continuum (e.g., Koshida et al. 2014). In that case, our approximation will tend to overestimate continuum visibilities, leading to a $\approx 10 - 20\%$ underestimate of the continuum size.

These measurements require deep integrations, but do not suffer from systematic errors related to calibration or coherence loss. We measure V_c from this method in 4 sources (3C 273, PDS 456, NGC 3783, IRAS 09149-6206). We expect V_c to be independent over line spectral channel. From Equation 2, we then

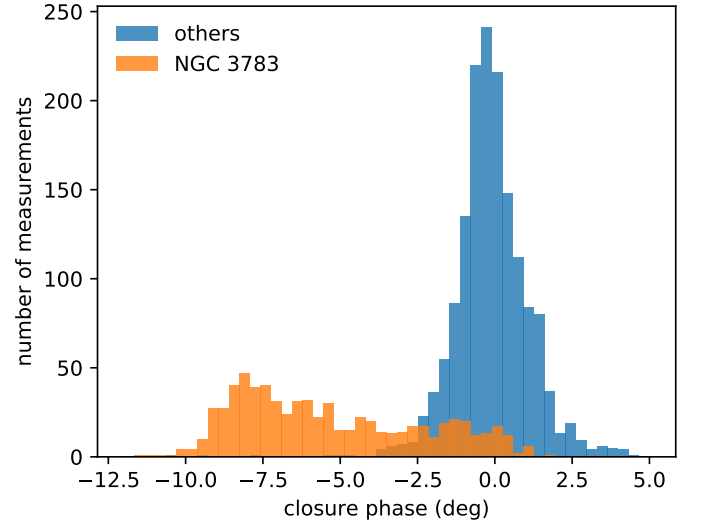


Fig. 5. Distributions of measured closure phases for NGC 3783 (orange) and other AGN targets with sufficient data (3C 273, PDS 456, Mrk 509, IRAS 09149-6206).

predict an amplitude signature $|v|$ which follows the shape of the spectral line, with a peak at the peak of the line where the contrast between line and continuum images is largest. An example is shown in Figure 3 for PDS 456, where the visibility amplitude averaged over long baselines shows a significant increase at the spectral line, following the expected behavior.

Sample comparisons of our independent FT continuum and SC differential measurements of the continuum visibility amplitude V_c are shown in Figure 4. They are generally consistent. Following our analysis of the FT data, we also perform single 1D Gaussian source fits to the SC differential data for each source to infer a characteristic FWHM size.

4. Results

4.1. Elongation and asymmetry

We do not find evidence for 2D (elongated) or asymmetric structure in either the SC or FT data, except in NGC 3783, which will be analyzed in more detail elsewhere. Figure 5 shows distributions of closure phases combined for 3C 273, PDS 456, IRAS 09149-6206, and Mrk 509 (our sources with the most and highest precision data). The closure phase is formed by summing the visibility phase over baseline triangles, and is immune to telescope-based phase errors. The distributions show a typical closure phase rms of $\pm 1^\circ$ with a median consistent with zero, indicating symmetric structure down to < 0.1 mas scales.² The closure phases measured for NGC 3783 are shown as a separate histogram, are always $< 0^\circ$, and clearly indicative of asymmetry. For consistency with the other sources, we report size measurements for NGC 3783 from 1D Gaussian model fits, even though the model is inconsistent with the observed non-zero closure phases.

4.2. The hot dust is more extended than the BLR

In all sources where we detect a differential amplitude signature, the amplitude increases at the line, showing robustly that the broad emission line region is more compact than the hot dust continuum. In the remaining targets we were limited by sensitivity, e.g. the size difference is not constraining. We confirm that the hot dust emission region is much larger than the BLR, as inferred from past reverberation and spectral measurements (e.g., Netzer 2015, and references therein). In 3C 273 we also have an interferometric BLR radius measured from kinematic modeling of the detected velocity gradient in differential phase data (Gravity Collaboration et al. 2018), which is a factor ≈ 3 smaller than that of the hot dust.

4.3. Hot dust size measurements

FWHM 1D Gaussian size measurements for each source are shown in Figure 6 and listed in Table 2 for the FT and where available also the SC measurements. All sources are partially resolved with sizes $\lesssim 1$ mas, and as compact as ≈ 0.3 mas (3C 273). Such small sizes relative to the VLTI interferometric beam are still detected due to the high sensitivity and improved uv-coverage of GRAVITY. The sizes measured by the SC and FT methods are generally consistent. The scatter in our size measurements is dominated by systematic calibration errors, which cause scatter in the sizes measured in individual exposures that are much larger than expected by the signal-to-noise of the individual V^2 measurements. This is reflected in the scatter of their zero baseline visibilities V_0 .

Past NIR interferometry measured sizes using a thin ring (delta function) intensity distribution rather than a Gaussian as we have done here. Keck Interferometer observations found a hot dust radius of the quasar 3C 273 of 0.25 ± 0.1 mas assuming a thin ring model (Kishimoto et al. 2011a), which is equivalent to a Gaussian HWHM of 0.21 ± 0.09 mas and consistent with our Gaussian HWHM result of 0.15 ± 0.03 mas. VLTI/AMBER observations found a thin ring radius of 0.74 ± 0.23 mas for NGC 3783 (Gaussian HWHM of 0.56 ± 0.17 mas), consistent

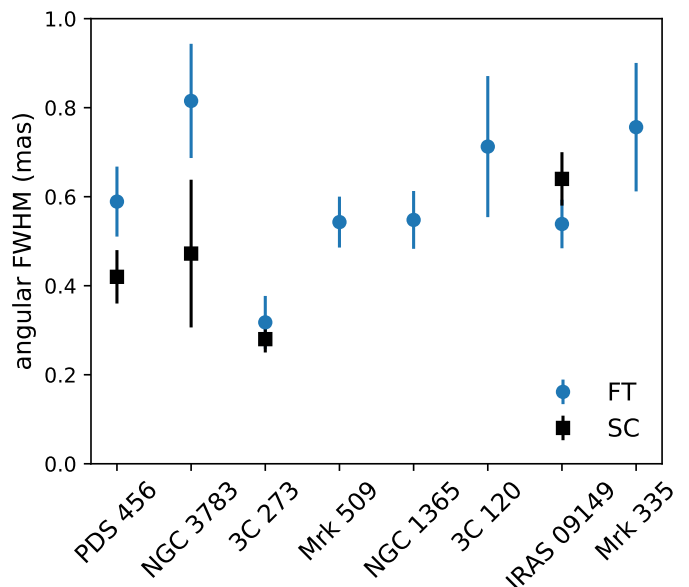


Fig. 6. Average source angular sizes (Gaussian FWHM) and their uncertainties measured from both continuum (FT) and spectral differential (SC) data. The latter are measured in deep integrations and are only possible for 4 objects so far.

with our result of 0.42 ± 0.06 mas. We note that the Keck observations used only 1 baseline (compared to our 6), while the VLTI/AMBER data used 3 baselines but at lower signal-to-noise. In analyzing the AMBER data, Weigelt et al. (2012) further assumed a fixed zero baseline visibility of unity.

4.4. BLR size estimates

We have inferred continuum visibilities and sizes from SC differential data by assuming a point source BLR ($V_l = 1$). Alternatively, we can take the measured size from the FT data and use the SC differential data to infer the BLR size. For 3C 273, this gives $R_{\text{BLR}} = 75 \pm 65 \mu\text{as}$, consistent with both GRAVITY modeling of the SC differential phases (Gravity Collaboration et al. 2018) and various estimates from reverberation mapping (Kaspi et al. 2000; Peterson et al. 2004; Zhang et al. 2019). For IRAS 09149-6206, the result is an upper limit of $R_{\text{BLR}} \lesssim 100 \mu\text{as}$. For PDS 456 and NGC 3783, taken at face value we would obtain large BLR sizes $R_{\text{BLR}} = 200 \pm 70 \mu\text{as}$ and $R_{\text{BLR}} = 320 \pm 100 \mu\text{as}$. The uncertainties are large because the SC differential amplitude is weakly sensitive to BLR size for such small angular sizes relative to the baseline resolution. We also note that any systematic offsets between our FT and SC results would likely change the results by a large amount compared to the statistical uncertainty. Still, in principle combining FT and SC data with sufficient sensitivity provides a model-independent measurement of BLR size that does not rely on adopting a kinematic model of the broad emission line profile.

5. Discussion

We have measured the K-band continuum sizes of 8 bright Type 1 AGN using near-infrared interferometry with the VLTI instrument GRAVITY. We use continuum visibilities as measured by the GRAVITY fringe tracker V^2 , and from the spectral differential visibility amplitudes. Each source is partially resolved, with FWHM sizes $\approx 0.3 - 0.8$ mas smaller than the VLTI beam ≈ 4 mas. We find no evidence for significant elongation or asymme-

² In the partially resolved limit the closure phase is to leading order $\propto (2\pi u \cdot x)^3$ where x is the size scale of the image (Lachaume 2003). This becomes extremely small for sizes < 0.1 mas regardless of intrinsic source structure.

Table 2. Source zero baseline visibilities, angular and physical size measurements, dust surface emissivities, and bolometric luminosities. Angular sizes are reported as Gaussian FWHM, while for consistency with the literature physical radii are measured for a thin ring model assuming a 20% point source fraction.

source	FT V_0	FT size (mas)	SC size (mas)	radius (pc)	emissivity	$\log L_{\text{bol}}$
PDS 456	0.98 ± 0.02	0.59 ± 0.08	0.42 ± 0.06	1.342 ± 0.179	0.13 ± 0.03	47.00
NGC 3783	0.86 ± 0.05	0.82 ± 0.13	0.47 ± 0.17	0.110 ± 0.017	0.11 ± 0.03	44.52
3C 273	0.95 ± 0.03	0.32 ± 0.06	0.28 ± 0.03	0.567 ± 0.106	0.71 ± 0.27	46.64
Mrk 509	0.86 ± 0.01	0.54 ± 0.06	...	0.249 ± 0.026	0.13 ± 0.03	45.31
NGC 1365	0.98 ± 0.01	0.55 ± 0.06	...	0.032 ± 0.004	0.24 ± 0.06	42.96
3C 120	0.93 ± 0.03	0.71 ± 0.16	...	0.318 ± 0.071	0.03 ± 0.01	45.28
IRAS 09149-6206	0.85 ± 0.02	0.54 ± 0.05	0.64 ± 0.06	0.405 ± 0.041	0.30 ± 0.06	45.29
Mrk 335	0.92 ± 0.02	0.44 ± 0.12	...	0.155 ± 0.041	0.14 ± 0.07	44.80

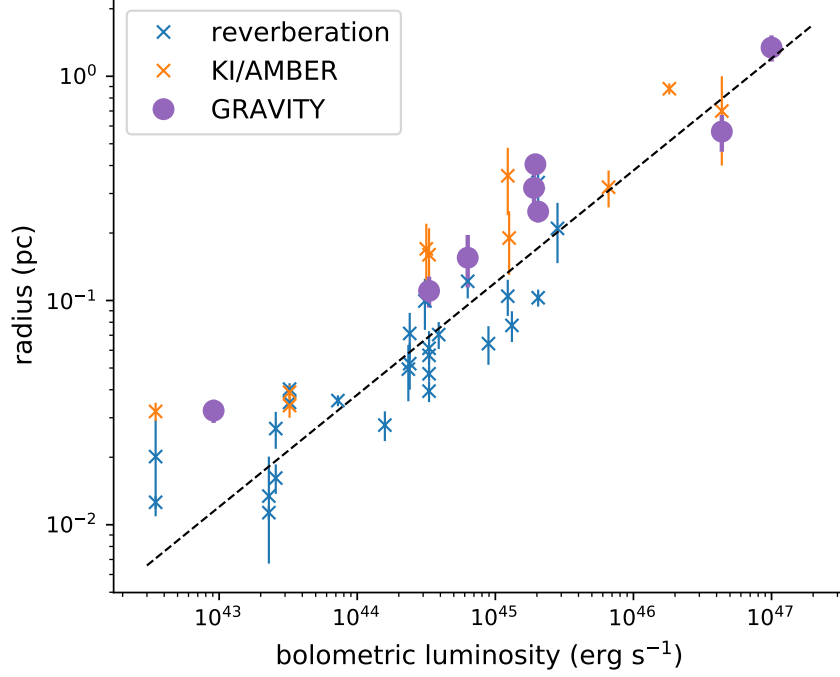


Fig. 7. Radius–luminosity relation for literature reverberation and interferometry size measurements (blue and orange x’s) compared to our new GRAVITY measurements (filled circles). The dashed line is the best fitting $R \sim L^{1/2}$ fit to reverberation measurements (Suganuma et al. 2006; Koshida et al. 2014). We use FT measurements and our own bolometric luminosity estimates in all cases. The radii reported here for all interferometry measurements is that of a thin ring with an assumed unresolved point source flux fraction of 20% (see subsection 5.2 for details).

Table 3. Reverberation lags, interferometric thin ring radii, and inferred geometric distances compared to fiducial ones given the AGN redshift. For NGC 3783, we have used the smaller size derived from differential SC data.

source	lag (lt-d)	R_{ring} (mas)	D_A (Mpc)	$D_{A,\text{fiducial}}$ (Mpc)
Mrk 335	148.9 ± 24.1	0.29 ± 0.08	90.0 ± 27.8	109.0
NGC 3783	73.0 ± 14.0	0.32 ± 0.11	39.8 ± 15.9	41.6
Mrk 509	126.8 ± 11.0	0.36 ± 0.04	62.3 ± 8.5	141.0

try in 7 of 8 targets observed. We confirm that the BLR is more compact than the hot dust emission from direct measurements of the spectral differential visibility amplitude. Here we discuss the implications of our results for the size, structure, and physical properties of hot dust near AGN.

5.1. Hot dust surface emissivity

We measure the hot dust surface emissivity $\epsilon_v \equiv I_v/B_v$ (product of grain emissivity and surface filling factor) for objects in our sample, assuming a true dust temperature $T = 1500$ K (Table 2). This metric is equivalent to the surface brightness reported by Kishimoto et al. (2011b). Since our range of angular sizes is

mostly consistent with past work, the dust surface emissivity values are as well $\epsilon_v \approx 0.1 - 0.2$. The compact angular size of 3C 273 leads to a higher emissivity.

Since we do not resolve the emission region, our inferred values correspond to averages over the effective VLTI beam, and are lower limits to the peak hot dust emissivity. The correction could be large, if a significant amount of the K band emission originates in a narrow ring (Kishimoto et al. 2009, Gravity Collaboration et al., submitted). Such large surface emissivities close to blackbody emission can be expected if the dust emission is dominated by large grains $\gtrsim 0.2 \mu\text{m}$ as compared to a standard ISM grain size distribution with mean grain size $< 0.1 \mu\text{m}$. This is

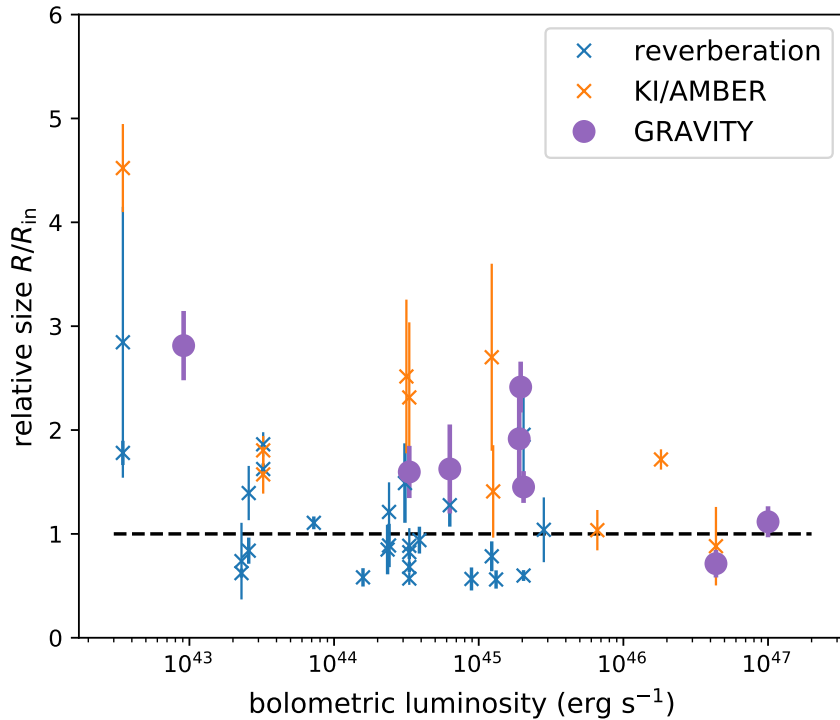


Fig. 8. Radius from GRAVITY and Keck/AMBER near-infrared interferometry, measured relative to the empirical radius-luminosity relation from reverberation mapping (Suganuma et al. 2006; Koshida et al. 2014). Reverberation sizes are shown for comparison and the error bars correspond to 1σ in all cases. Both interferometry data sets show a larger median size $R/R_{\text{in}} > 1$ and decreasing relative size with increasing luminosity, particularly evident as $R/R_{\text{in}} \lesssim 1$ for quasars.

consistent with differential grain sublimation in the AGN vicinity (Hönig & Kishimoto 2017).

5.2. The hot dust radius-luminosity relation

Reverberation (Glass 1992; Suganuma et al. 2006; Koshida et al. 2014) and near-infrared interferometry (Kishimoto et al. 2009, 2011a; Weigelt et al. 2012) observations have used hot dust continuum sizes to measure a radius-luminosity relation, $R \sim L^{1/2}$, consistent with the scaling for hot dust originating near the sublimation radius. At the same time, the normalization of that relation indicates a more compact than expected dust region, perhaps explained by the presence of large graphite grains (Kishimoto et al. 2007). A relationship $R \sim L^{1/2}$ predicts equal angular size at constant observed flux (e.g., Elvis & Karovska 2002). Here all objects are $K \approx 10$, and their relatively constant angular sizes $\approx 0.3 - 0.8$ mas over 4 orders of magnitude in bolometric luminosity show that the physical radius is indeed increasing with luminosity.

Our observations nearly double the size of the near-infrared interferometry sample, and are measured with significantly improved uv-coverage and sensitivity. For comparison with past work, we measure physical radii by converting our Gaussian HWHM measurements to thin ring angular radii (divide by a factor of $\sqrt{\ln 2} \approx 0.8$). We then convert to a physical radius using the angular diameter distances to our targets. Significant point source contributions to the NIR source (from the accretion disk and/or jet) could cause us to underestimate the hot dust size. In the partially resolved limit, the source size corresponds to the normalized second moment of the image. Then the apparent source size for a point source plus extended model can be written,

$$\sigma_{\text{app}}^2 = f_{\text{pt}}\sigma_{\text{pt}}^2 + (1 - f_{\text{pt}})\sigma_{\text{true}}^2, \quad (4)$$

$$\frac{\sigma_{\text{app}}}{\sigma_{\text{true}}} \approx \sqrt{1 - f_{\text{pt}}}, \quad (5)$$

where σ are normalized second moments for the point source component ($\sigma_{\text{pt}} = 0$), the total apparent source, and the true hot dust component. The fractional point source flux, f_{pt} , varies per object. We adopt a typical constant value $f_{\text{pt}} = 0.2$ in converting to physical radius (Kishimoto et al. 2007), which results in a size increase of $\approx 10\%$. The bolometric luminosities of both our objects and those from the literature are estimated uniformly as described in Appendix A. The physical thin ring radii and bolometric luminosity values used are listed in Table 2.

Figure 7 shows the resulting physical hot dust emission radius vs. bolometric luminosity from past and our new measurements. Fitting a power law $R \sim L_{\text{bol}}^{1/2}$ to reverberation measurements from the literature (Suganuma et al. 2006; Kishimoto et al. 2007; Koshida et al. 2014), we obtain the dashed line with a normalization $R_{44} = 0.038 \pm 0.02$ pc, where R_{44} is the radius $c\Delta t$ at a bolometric luminosity of $10^{44} \text{ erg s}^{-1}$ and Δt is the measured lag between the K and V bands (e.g., Koshida et al. 2014). Leaving the slope free, we find a best fit with a flatter luminosity-dependence, $R \sim L_{\text{bol}}^{0.40 \pm 0.04}$. The individual data points are plotted as blue x's. Combining the Seyfert galaxies in our sample ($L_{\text{bol}} \lesssim 10^{46} \text{ erg s}^{-1}$) with past KI/AMBER results, we find a similar best fitting radius-luminosity relation from NIR interferometry as from reverberation. The two luminous quasars ($L_{\text{bol}} > 10^{46} \text{ erg s}^{-1}$, PDS 456 and especially 3C 273) show smaller hot dust angular sizes than the other sources. Those sizes are robust, obtained with both SC and FT data, and precise (uncertainties $\lesssim 20\%$). The measurement for 3C 273 agrees with that reported by Kishimoto et al. (2009). We generally find that

interferometry sizes are larger than those from reverberation at comparable bolometric luminosity, in agreement with past work (e.g., Kishimoto et al. 2011a; Koshida et al. 2014).

Figure 8 shows NIR interferometry radius measurements scaled to the $R - L$ relation from reverberation. The scatter between objects is larger than their errors, showing that there are differences in viewing geometry and/or physical structure (geometry or dust composition). At low luminosities, the interferometry sizes are systematically above the relation. Larger interferometric sizes might be expected as a result of an extended NIR emission region due to their weighting by total intensity, rather than by the response to a variable central source (e.g., Koratkar & Gaskell 1991). Kishimoto et al. (2011b) argued that the reverberation value corresponds to the sublimation radius, R_{in} , and that values $R/R_{\text{in}} \approx 1$ imply a hot dust emissivity falling rapidly away from that location. Larger values instead correspond to a shallower emissivity. In Figure 8 we see that R/R_{in} falls with increasing bolometric luminosity, if with significant scatter. One explanation is a variable radial dust emission profile, which is sharply peaked at the sublimation radius for more luminous objects and slightly more extended at lower luminosity. Our data show more compact hot dust at high luminosity, and support this interpretation.

5.3. Compact hot dust in quasars

The two luminous sources also have $L/L_{\text{Edd}} \sim 1$ and could have particularly high point source flux contributions. A bias by a factor of 2, needed to bring 3C 273 within the observed range of other objects, requires a point source fraction $f_{\text{pt}} = 3/4$, e.g. the observed K band emission needs to be dominated by contaminating emission. Kishimoto et al. (2011a) estimate an accretion disk contribution for 3C 273 of $f_{\text{pt}} \approx 0.3$, similar to our assumed $f_{\text{pt}} = 0.2$. Non-thermal jet emission could also contribute in the NIR, as seen in rapidly variable K band light curves (e.g., Robson et al. 1993; McHardy et al. 2007; Bewketu Belete et al. 2018) corresponding to flaring events. Our observations of 3C 273 have produced consistent acquisition camera H band magnitudes and size measurements from July 2017 to May 2018. The acquisition camera H band flux density of ≈ 40 mJy is consistent with the quiescent state of 3C 273 with no evidence of flare contributions (e.g., Robson et al. 1993; Soldi et al. 2008). Robson et al. (1993) estimate a jet contribution to the quiescent flux density of ≈ 30 mJy from extrapolating the power law spectral slope seen at millimeter wavelengths. Soldi et al. (2008) find a significant accretion disk fraction but a much smaller jet contribution in SED fitting due to an imposed spectral cutoff to the synchrotron spectrum. Kishimoto et al. (2011a) estimate this contribution as $\lesssim 8$ mJy based on the low NIR polarization fraction and assuming an intrinsic $\approx 10\%$ net polarization for the synchrotron component. These estimates produce a wide range of possible point source flux fractions from jet emission (assuming a small jet emission size), $f_{\text{jet}} \approx 0.1 - 0.4$. Combining the highest inferred values for both the accretion disk and jet contributions, the total point source contribution could plausibly be large enough to explain our observed compact size. A total point source contribution $\lesssim 0.5$ seems more likely based on the clear thermal dust bump in the NIR SED (Soldi et al. 2008), and would increase our hot dust size by $\lesssim 20\%$. PDS 456 also shows a compact size and is radio quiet. We conclude that contaminating emission can contribute to the compact sizes we measure, particularly for 3C 273, but probably does not explain our finding of $R/R_{\text{in}} \lesssim 1$ in two luminous quasars.

A further bias comes from errors in the bolometric luminosity estimates. Even random errors in L_{bol} will tend to produce an anti-correlation of R/R_{in} and L_{bol} , because $R_{\text{in}} \propto L^{1/2}$. By simulating many random data sets, we find that the degree of anti-correlation observed in GRAVITY and KI/AMBER data could be explained if the true luminosity errors are ≈ 0.6 dex. Our measured errors by comparing various methods appear to be somewhat smaller $\approx 0.3 - 0.5$ dex (Appendix A). Still this bias warrants caution in interpreting the results in terms of varying hot dust structure with source luminosity.

5.4. Geometric distance estimates

Past measurements of the hot dust radius from reverberation have been made for NGC 3783 (Lira et al. 2011), Mrk 335, and Mrk 509 (Koshida et al. 2014). Geometric estimates of the angular diameter distance from combining time lags with interferometric sizes are given in Table 3. For those estimates we have followed Koshida et al. (2014) in assuming $R = c\Delta t = D_A\theta_{\text{ring}}$ where Δt is the reverberation lag and θ_{ring} is the angular radius of a thin ring model with a 20% unresolved point source contribution. We find consistent angular diameter distances to the fiducial values given the redshift for Mrk 335, as well as for NGC 3783 if we use its differential SC angular size. The GRAVITY inferred physical radius of Mrk 509 is a factor $\gtrsim 2$ larger than from reverberation, given its fiducial angular diameter distance. A similar discrepancy is found using the continuum FT size of NGC 3783, although that object clearly shows complex structure beyond a partially resolved thin ring. Understanding the discrepancy and the physical structure of the NIR emission region will be important for efforts to measure geometric distances by combining interferometric and reverberation sizes (Hönig et al. 2014).

6. Summary

We have reported near-infrared interferometry measurements of 8 AGN made with the second generation VLTI instrument GRAVITY. In all cases, we partially resolve the continuum hot dust emission region and can measure its size. In the 4 objects with sufficiently deep integrations, we use a new spectral differential method to show definitively that the hot dust continuum is much larger than the low-ionization Pa α or Br γ broad emission line region. In 7/8 objects, we see no clear evidence for elongation or asymmetry and in particular constrain the closure phases to $\lesssim 1^\circ$. The hot dust continuum sizes span $0.3 - 0.8$ mas, mostly consistent with past interferometry measurements with the Keck Interferometer and the VLTI instrument AMBER. Our objects span 4 orders of magnitude in bolometric luminosity with similar V magnitude. Their roughly constant angular size implies increasing physical radius with luminosity, consistent with past reverberation and interferometry measurements. We find that at low luminosity, the hot dust sizes are systematically larger than those from reverberation, potentially related to emission from an extended region. At high luminosity, the two quasars in our sample are compact, with sizes consistent with sharply peaked emission at the sublimation radius. Accretion disk and/or jet contributions to the flux and biases from errors in estimated bolometric luminosities are probably not sufficient to fully explain this finding.

Acknowledgements. J.D., M.B., and A.J.R. were supported by a Sofja Kovalevskaja award from the Alexander von Humboldt foundation and in part by NSF grant AST 1909711. SFH acknowledges support by the EU Horizon 2020 framework programme via the ERC Starting Grant DUST-IN-THE-WIND (ERC-2015-StG- 677117). M.K. acknowledges support from JSPS

(16H05731). F.E. and O.P. acknowledge support from ERC synergy grant No. 610058 (Black-HoleCam). A.A. and P.G. acknowledge funding from Fundação para a Ciência e a Tecnologia through grants UID/FIS/00099/2013 and SFRH/BSAB/142940/2018. P.O.P acknowledges support from the Programme National Hautes Energies (PNHE) of the Centre National de la Recherche Scientifique (CNRS).

Appendix A: Bolometric luminosity

The bolometric luminosity of the AGNs are estimated mainly with X-ray measurements. Unless noted in particular, we take the 14–195 keV flux from the BAT AGN Spectroscopic Survey (Koss et al. 2017), taken directly from the 70-month Swift-BAT survey (Baumgartner et al. 2013). The hard X-ray emission is less contaminated by the host galaxy and less affected by the absorption. We adopt the luminosity dependent bolometric correction relation provided by Winter et al. (2012),

$$\log \left(\frac{L_{\text{bol}, 14-195 \text{ keV}}}{\text{erg s}^{-1}} \right) = 1.1157 \log \left(\frac{L_{14-195 \text{ keV}}}{\text{erg s}^{-1}} \right) - 4.2280. \quad (\text{A.1})$$

We also collect their optical (5100 Å) continuum from BAT catalog and 12 μm nuclear emission from Asmus et al. (2014) to confirm the consistency of different methods to derive the bolometric luminosity. Following the 5100 Å bolometric correction of Trakhtenbrot et al. (2017), we use,

$$\log \left(\frac{L_{\text{bol}, 5100 \text{ Å}}}{\text{erg s}^{-1}} \right) = 0.916 \log \left(\frac{\nu L_{\nu}(5100 \text{ Å})}{\text{erg s}^{-1}} \right) + 4.596. \quad (\text{A.2})$$

For the MIR data, we first convert the 12 μm flux to 2–10 keV intrinsic flux according to Asmus et al. (2011),

$$\log \left(\frac{f_{2-10 \text{ keV}}}{\text{mJy}} \right) = 0.89 \log \left(\frac{f_{12 \mu\text{m}}}{\text{mJy}} \right) - 12.81. \quad (\text{A.3})$$

Then we convert 2–10 keV luminosity to 14–195 keV luminosity according to Winter et al. (2009),

$$\log \left(\frac{L_{14-195 \text{ keV}}}{\text{erg s}^{-1}} \right) = 0.94 \log \left(\frac{L_{2-10 \text{ keV}}}{\text{erg s}^{-1}} \right) + 2.91, \quad (\text{A.4})$$

and rely on the 14–195 keV bolometric correction (Winter et al. 2012) to obtain the final bolometric luminosity. The latter step is to maintain consistency with our X-ray bolometric luminosity. The intrinsic scatter of the relation in Equation (A.4) may introduce additional uncertainty. However, we believe this is not as important considering the large uncertainty of the bolometric correction (see below). We compare the bolometric luminosities derived from the three methods in Figure A.1. The scatters of the relations are ~ 0.3–0.5 dex, which is likely reflecting the uncertainty of the bolometric correction methods at a single frequency. Considering the source variability and the difference of their intrinsic SEDs, the uncertainty of our bolometric correction is hardly below ~ 0.5 dex (see Netzer 2019 and discussion therein). Therefore, we conclude that the three methods produce mostly consistent results. A few objects are noted individually as follows, including the four objects (PDS 456, Mrk 231, IRAS 13349+2438, PG 1202+281) which are not available in the BAT AGN sample.

Mrk 335: It is reported extremely variable in X-ray with amplitude a factor of ~ 10 and timescale tens of days (Grupe et al. 2012). Therefore, we prefer to adopt the 5100 Å bolometric luminosity, which is consistent with the value reported by Woo & Urry (2002), who calculated the bolometric luminosity by integrating the observed flux over the SED.

3C 120: The bolometric luminosity derived from 5100 Å luminosity is about 1 order of magnitude lower than those with other methods. This is possibly due to variability. However, we note that the 5100 Å luminosity reported by Vestergaard & Peterson (2006) is ~ 0.9 dex higher than that of the BAT AGN Spectroscopic Survey. The former provides a bolometric luminosity

more consistent with our other methods. The X-ray derived bolometric luminosity is also consistent with that integrated over the SED from Woo & Urry (2002).

3C 273: The jet emission is likely contributing significantly to the X-ray luminosity of 3C 273 (Dermer et al. 1997; Vasudevan & Fabian 2007). Therefore, we discard the bolometric luminosities derived from X-ray data and adopt the value based on 5100 Å, which is found to be consistent with that based on 12 μm data. *PDS 456*: This source is very luminous in UV/optical. Its 5100 Å luminosity is ~ $2 \times 10^{46} \text{ erg s}^{-1}$ (Simpson et al. 1999; Reeves et al. 2009), corresponding to $L_{\text{bol}, 5100 \text{ Å}} = 1.0 \times 10^{47} \text{ erg s}^{-1}$. This is very well consistent with the bolometric luminosity derived from UV–IR SED (Simpson et al. 1999). PDS 456 is extremely variable in X-ray (Reeves et al. 2002) and the observed 2–10 keV luminosity is only 0.2% of the bolometric luminosity (Reeves et al. 2009). Therefore, we do not quote the bolometric luminosity estimated from X-rays.

Mrk 231: Recent *NuSTAR* measurements reveal Mrk 231 to be intrinsically X-ray weak (Teng et al. 2014). Therefore, X-ray measurements are not suitable for deriving the bolometric luminosity for this target. We adopt the 12 μm measurement from Lopez-Rodriguez et al. (2017) and obtain the bolometric luminosity ~ $6.6 \times 10^{45} \text{ erg s}^{-1}$, which is consistent with the bolometric luminosity, $4\text{--}5 \times 10^{45} \text{ erg s}^{-1}$, derived from the decomposition of IR SED (Farrah et al. 2003; Teng et al. 2014).

IRAS 13349+2438: We derive the bolometric luminosity of IRAS 13349+2438, ~ $1.8 \times 10^{46} \text{ erg s}^{-1}$, based on 12 μm data. This is within a factor of 2 consistent with the estimates based on quasar SEDs (Beichman et al. 1986; Lee et al. 2013).

IC 4329A: The bolometric luminosity derived from X-ray data is ~ 0.9 dex higher than that from 5100 Å. This is likely reflecting the uncertainty of the different bolometric luminosity corrections. The 5100 Å luminosity of BAT catalog is consistent with other measurements (e.g., Bentz et al. 2009). Meanwhile, the X-ray bolometric luminosity is consistent with the values derived from the AGN SEDs (Woo & Urry 2002; Vasudevan et al. 2010). Therefore, we still adopt the X-ray derived bolometric luminosity in our analysis. It is worth noting that, with the bolometric correction theoretically calculated by Netzer (2019), the bolometric luminosity based on 5100 Å luminosity is ~ 0.4 dex higher than what we quote, and as a result is more consistent with that derived from X-rays.

PG 1202+281: We collect the 5100 Å data from Vestergaard & Peterson (2006). The derived the bolometric luminosity is well consistent with that derived from NIR-to-X-ray SED (Runnoe et al. 2012).

Mrk 744: Our X-ray derived bolometric luminosity is well consistent with that reported in Woo & Urry (2002) interpolating the AGN SED.

Mrk 110: We collect the 5100 Å luminosity from Vestergaard & Peterson (2006).

IRAS 03450+0055: The 5100 Å luminosity comes from Afanasiev et al. (2019).

References

- Afanasiev, V. L., Popović, L. Č., & Shapovalova, A. I. 2019, MNRAS, 482, 4985
- Antonucci, R. 1993, ARA&A, 31, 473
- Asmus, D., Gandhi, P., Smette, A., Hönig, S. F., & Duschl, W. J. 2011, A&A, 536, A36
- Asmus, D., Hönig, S. F., Gandhi, P., Smette, A., & Duschl, W. J. 2014, MNRAS, 439, 1648
- Barvainis, R. 1987, ApJ, 320, 537

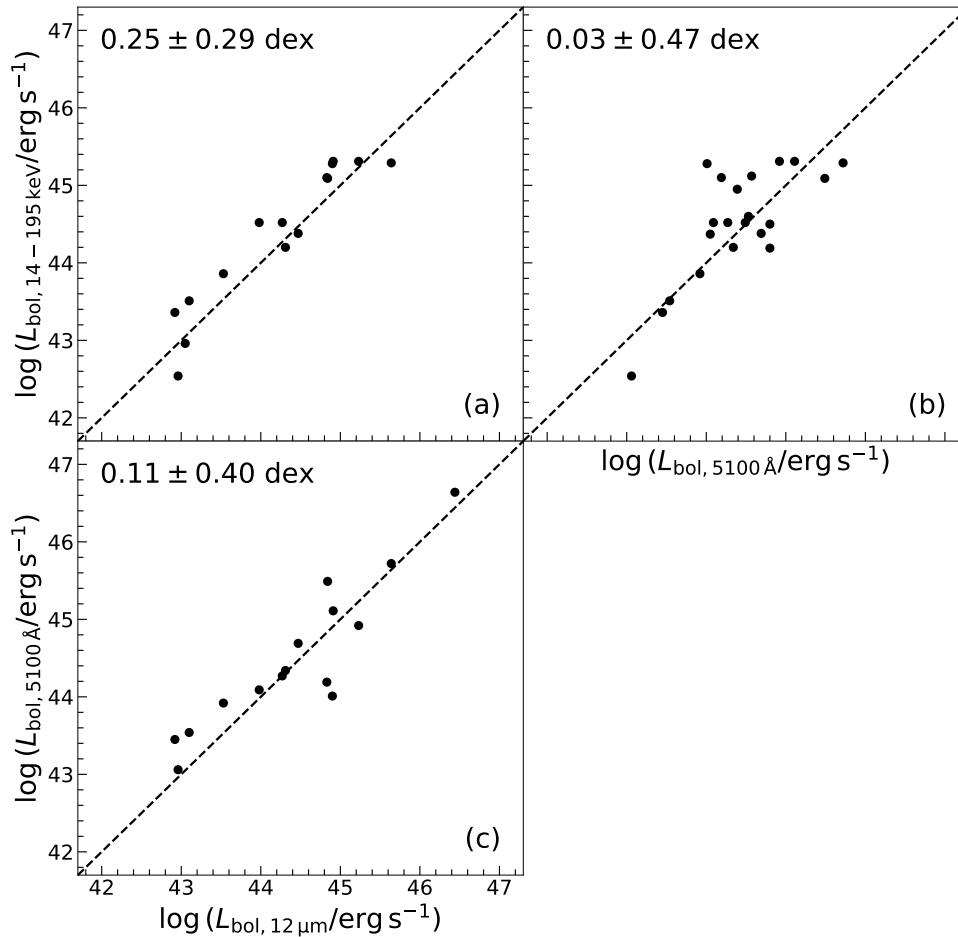


Fig. A.1. Comparison of AGN bolometric luminosities derived using the different methods listed in Table A.1. The median and standard deviation of the difference ($y - x$) are indicated in the upper left corner of each panel. The dashed lines indicate the one-to-one relation. (a) The 14–195 keV and 12 μm results show a possible offset, comparable to their scatter (≈ 0.3 dex). The 5100 Å bolometric luminosity tends to be better consistent with both 14–195 keV (b) and 12 μm (c), although the scatters of both relations are considerable. Considering the uncertainty of the bolometric correction is large (~ 0.5 dex), the different methods are relatively well consistent with each other.

- Baumgartner, W. H., Tueller, J., Markwardt, C. B., et al. 2013, *ApJS*, 207, 19
- Beichman, C. A., Soifer, B. T., Helou, G., et al. 1986, *ApJ*, 308, L1
- Bentz, M. C., Peterson, B. M., Netzer, H., Pogge, R. W., & Vestergaard, M. 2009, *ApJ*, 697, 160
- Bewketu Belete, A., Bravo, J. P., Canto Martins, B. L., et al. 2018, *arXiv e-prints*, arXiv:1805.07287
- Dermer, C. D., Sturmer, S. J., & Schlickeiser, R. 1997, *ApJS*, 109, 103
- Elvis, M. & Karovska, M. 2002, *ApJ*, 581, L67
- Farrah, D., Afonso, J., Efstathiou, A., et al. 2003, *MNRAS*, 343, 585
- Glass, I. S. 1992, *MNRAS*, 256, 23P
- Gravity Collaboration, Abuter, R., Accardo, M., et al. 2017, *A&A*, 602, A94
- Gravity Collaboration, Sturm, E., Dexter, J., et al. 2018, *Nature*, 563, 657
- Grupe, D., Komossa, S., Gallo, L. C., et al. 2012, *ApJS*, 199, 28
- Hönig, S. F. & Kishimoto, M. 2017, *ApJ*, 838, L20
- Hönig, S. F., Watson, D., Kishimoto, M., & Hjorth, J. 2014, *Nature*, 515, 528
- Johnson, M. D., Narayan, R., Psaltis, D., et al. 2018, *ApJ*, 865, 104
- Kaspi, S., Smith, P. S., Netzer, H., et al. 2000, *ApJ*, 533, 631
- Kishimoto, M., Hönig, S. F., Antonucci, R., et al. 2011a, *A&A*, 527, A121
- Kishimoto, M., Hönig, S. F., Antonucci, R., et al. 2009, *A&A*, 507, L57
- Kishimoto, M., Hönig, S. F., Antonucci, R., et al. 2011b, *A&A*, 536, A78
- Kishimoto, M., Hönig, S. F., Beckert, T., & Weigelt, G. 2007, *A&A*, 476, 713
- Koratkar, A. P. & Gaskell, C. M. 1991, *ApJS*, 75, 719
- Koshida, S., Minezaki, T., Yoshii, Y., et al. 2014, *ApJ*, 788, 159
- Koss, M., Trakhtenbrot, B., Ricci, C., et al. 2017, *ApJ*, 850, 74
- Lachaume, R. 2003, *A&A*, 400, 795
- Lacour, S., Dembet, R., Abuter, R., et al. 2019, *A&A*, 624, A99
- Lapeyrere, V., Kervella, P., Lacour, S., et al. 2014, in *Society of Photo-Optical Instrumentation Engineers (SPIE) Conference Series*, Vol. 9146, Proc. SPIE, 91462D
- Lee, J. C., Kriss, G. A., Chakravorty, S., et al. 2013, *MNRAS*, 430, 2650
- Lira, P., Arévalo, P., Uttley, P., McHardy, I., & Breedt, E. 2011, *MNRAS*, 415, 1290
- López-Gonzaga, N., Burtscher, L., Tristram, K. R. W., Meisenheimer, K., & Schartmann, M. 2016, *A&A*, 591, A47
- Lopez-Rodriguez, E., Packham, C., Jones, T. J., et al. 2017, *MNRAS*, 464, 1762
- McHardy, I., Lawson, A., Newsam, A., et al. 2007, *MNRAS*, 375, 1521
- Millour, F., Petrov, R. G., Vannier, M., & Kraus, S. 2008, in *Society of Photo-Optical Instrumentation Engineers (SPIE) Conference Series*, Vol. 7013, Proc. SPIE, 70131G
- Netzer, H. 2015, *ARA&A*, 53, 365
- Netzer, H. 2019, *MNRAS*, 488, 5185
- Peterson, B. M., Ferrarese, L., Gilbert, K. M., et al. 2004, *ApJ*, 613, 682
- Reeves, J. N., O'Brien, P. T., Braito, V., et al. 2009, *ApJ*, 701, 493
- Reeves, J. N., Wynn, G., O'Brien, P. T., & Pounds, K. A. 2002, *MNRAS*, 336, L56
- Rieke, G. H. 1978, *ApJ*, 226, 550
- Robson, E. I., Litchfield, S. J., Gear, W. K., et al. 1993, *MNRAS*, 262, 249
- Runnoe, J. C., Brotherton, M. S., & Shang, Z. 2012, *MNRAS*, 426, 2677
- Simpson, C., Ward, M., O'Brien, P., & Reeves, J. 1999, *MNRAS*, 303, L23
- Soldi, S., Türler, M., Paltani, S., et al. 2008, *A&A*, 486, 411
- Suganuma, M., Yoshii, Y., Kobayashi, Y., et al. 2006, *ApJ*, 639, 46
- Swain, M., Vasisht, G., Akeson, R., et al. 2003, *ApJ*, 596, L163
- Teng, S. H., Brandt, W. N., Harrison, F. A., et al. 2014, *ApJ*, 785, 19
- Trakhtenbrot, B., Ricci, C., Koss, M. J., et al. 2017, *MNRAS*, 470, 800
- Urry, C. M. & Padovani, P. 1995, *PASP*, 107, 803
- Vasudevan, R. V. & Fabian, A. C. 2007, *MNRAS*, 381, 1235
- Vasudevan, R. V., Fabian, A. C., Gandhi, P., Winter, L. M., & Mushotzky, R. F. 2010, *MNRAS*, 402, 1081
- Vestergaard, M. & Peterson, B. M. 2006, *ApJ*, 641, 689
- Waisberg, I., Dexter, J., Pfuhl, O., et al. 2017, *ApJ*, 844, 72
- Weigelt, G., Hofmann, K. H., Kishimoto, M., et al. 2012, *A&A*, 541, L9

Source	D_L (Mpc)	$\log L_{\text{bol}, 14-195 \text{ keV}}$	$\log L_{\text{bol}, 12 \mu\text{m}}$	$\log L_{\text{bol}, 5100 \text{ \AA}}$	$\log L_{\text{bol}, \text{use}}$
NGC 1365	16.6	42.96	43.05	...	42.96
NGC 3783	47.8	44.52	44.27	44.27	44.52
Mrk 335	113.6	44.19	...	44.80	44.80
3C 120	144.9	45.28	44.90	44.01	45.28
Mrk 509	149.4	45.31	44.91	45.11	45.31
IRAS 09149–6206	254.7	45.29	45.64	45.72	45.29
3C 273	755.0	...	46.44	46.64	46.64
PDS 456	893.2	47.00	47.00
NGC 4051	13.4	42.54	42.96	43.06	42.54
NGC 4151	9.9	43.51	43.10	43.54	43.51
Mrk 231	185.6	...	45.82	...	45.82
IRAS 13349+2438	499.8	...	46.26	...	46.26
Mrk 6	82.6	44.50	...	44.80	44.50
Ark 120	140.4	45.09	44.84	45.49	45.09
IC 4329A	69.4	45.10	44.83	44.19	45.10
NGC 3227	18.8	43.36	42.92	43.45	43.36
NGC 7469	69.4	44.38	44.47	44.69	44.38
PG 1202+281	791.8	45.45	45.45
Fairall 9	203.9	45.31	45.23	44.92	45.31
Mrk 744	50.6	43.41	43.41
NGC 5548	73.8	44.52	43.98	44.09	44.52
Mrk 590	118.0	44.20	44.31	44.34	44.20
MCG +08–11–011	87.0	44.95	...	44.39	44.95
Mrk 79	95.8	44.52	...	44.49	44.52
Mrk 110	158.4	45.12	...	44.57	45.12
NGC 3516	51.5	44.37	...	44.05	44.37
NGC 4593	34.7	43.86	43.53	43.92	43.86
Mrk 817	138.2	44.60	...	44.53	44.60
IRAS 03450+0055	135.9	44.49	44.49

Table A.1. AGN distances and bolometric luminosities. All luminosities are in units of erg s^{-1} . (1) Source name. (2) Luminosity distance, calculated with $H_0 = 70 \text{ km s}^{-1}$, $\Omega_\Lambda = 0.7$, and $\Omega_M = 0.3$. (3) Bolometric luminosity derived from 14–195 keV data. The X-ray data come from BAT AGN Spectroscopic Survey (Baumgartner et al. 2013; Koss et al. 2017). (4) Bolometric luminosity derived from 12 μm data. The MIR data mainly come from Asmus et al. (2014), except that of Mrk 231 (see Appendix A). (5) Bolometric luminosity derived from optical 5100 \AA continuum data. The optical data mainly come from BAT AGN catalog, except for those of PDS 456 and PG 1202+281 (see Appendix A). (6) The bolometric luminosity that we adopt for the R – L relation. The 14–195 keV bolometric luminosities are preferred, unless the objects are noted individually.

Winter, L. M., Mushotzky, R. F., Reynolds, C. S., & Tueller, J. 2009, *ApJ*, 690, 1322

Winter, L. M., Veilleux, S., McKernan, B., & Kallman, T. R. 2012, *ApJ*, 745, 107

Woo, J.-H. & Urry, C. M. 2002, *ApJ*, 579, 530

Zhang, Z.-X., Du, P., Smith, P. S., et al. 2019, *ApJ*, 876, 49